Matching mechanical response for a MEMS vibratory tuning fork gyroscope

The Van Vu[1] [ORCID] · **Dung Quang Tran[1]** · **Trinh Duc Chu[2]**

Abstract

This paper introduces the configuration of the MEMS tuning fork gyroscope with the connecting diamond-shaped frame to achieve the anti-phase mode in the driving direction. The connecting frame is an important element to compensate for the phase deviation in two major directions in case of appearing elements that cause the phase deviation in operating such as driving force, geometric error,… The matching phase between the two tines of the TFG with this configuration is 89% and 93.67% in the driving and sensing mode, respectively. Even, the phase compensation ability of the system reaches up to 95.6% in the driving mode with increasing the equivalent stiffness of the connecting frame to four times.

1 Introduction

Based on the advancement of micro-electro-mechanical system (MEMS) technology, micro-machined vibratory gyroscopes (MVGs) has been becoming popular in technology science and real-life thanks to its advantages over traditional gyroscopes such as small size, light weight, and low power consumption (Yazdi et al. 1998; Dunzhu et al. 2014; Andrei 2006; Acar 2009; Andrei 1999). This device is a kind of micro-sensor used to detect and determine the angular velocity or rotational angle of a body into which the MVG is integrated. The MVG operates based on the "Coriolis effect" to transfer energy from the primary vibration to a secondary one (Acar 2009). These vibrations are in two perpendicular directions and called the driving and sensing direction respectively.

Tuning fork gyroscope (TFG) is known as an anti-phase system with the purpose to cancel the common-mode inputs (Acar 2009). The TFG structure consists of two identical masses connected directly or indirectly by a mechanical frame. The masses are driven in opposite directions but along the same axis (anti-phase mode). When external angular velocity in the vertical axis is applied, the secondary motion of the masses occurs in opposite directions as well. This state increases significantly the performance of TFG (Apostolyuk and Tay 2005; Bumkyoo et al. 2008; Guan et al. 2016). However, the traditional MEMS tuning fork structure with the direct mechanical coupling between two tines likely causes an in-phase vibratory mode (Guan et al. 2016), also could appear some errors in vibration (Yoon et al. 2012), (Weinberg and Kourepenis 2006). Therefore, TFG should be designed with the mechanical frame to guarantee the anti-phase mode in both the driving and sensing direction.

The mechanical frame connecting indirectly two tines in the TFG were designed in a diamond-shaped frame (Guan et al. 2016a, b), a U-shaped bar (Guan et al. 2014), a lozenge-shaped frame (Trinh et al. 2014), a structurally forced lever bar (Trusov et al. 2013), a T-shaped bar (Sharma et al. 2004; Zaman et al. 2008), or a straight linkage bar (Huilin and Yongpeng 2011). These researches focused on simulation and modal analysis to determine the frequency of anti-phase mode and the output characteristics of the TFG model. The results showed that the connecting frame is used to reject the vibration output and take likely the anti-phase mode. However, how the masses of the TFG respond when the external forces applied to them with the considered phase deviation has not been still studied yet. Besides, the response of the sense masses in TFG with the different forms of outside angular velocity should be considered.

This paper presents a TFG model with a connecting diamond-shaped frame to create and guarantee anti-phase mode in the first mode. Besides, the dynamic response of

✉ The Van Vu
  vuvanthe@mta.edu.vn

[1] Le Quy Don Technical University, Hanoi, Vietnam

[2] Vietnam National University, Hanoi, Vietnam

the device in the driving and sensing direction is analyzed to determine the anti-phase frequency and demonstrate the matching phase between two masses in two tines of this TFG. The output mechanical signals of the TFG also are studied by using a numerical analysis method in this research.

2 Configuration

The simple configuration of the proposed TFG is shown in Fig. 1. It consists of two tines. Each tine is defined as a single gyroscope and includes a proof-mass 1 and an outer frame 2. The configuration and dynamic characteristics of every single gyroscope are provided in (Van Vu et al. 2018). This outer frame is connected to the proof-mass by four elastic beams 3 and suspended on substrate thanks to

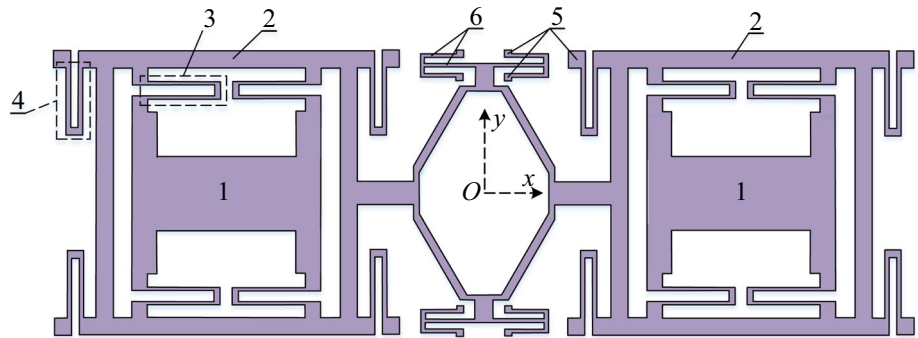**Fig. 1** 3D model of the proposed TFG with a diamond-shaped frame

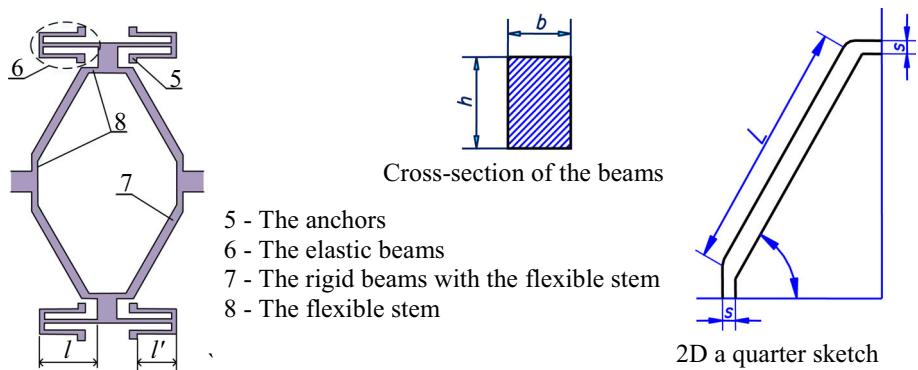**Fig. 2** Configuration and dynamic of the connecting frame with the diamond shape
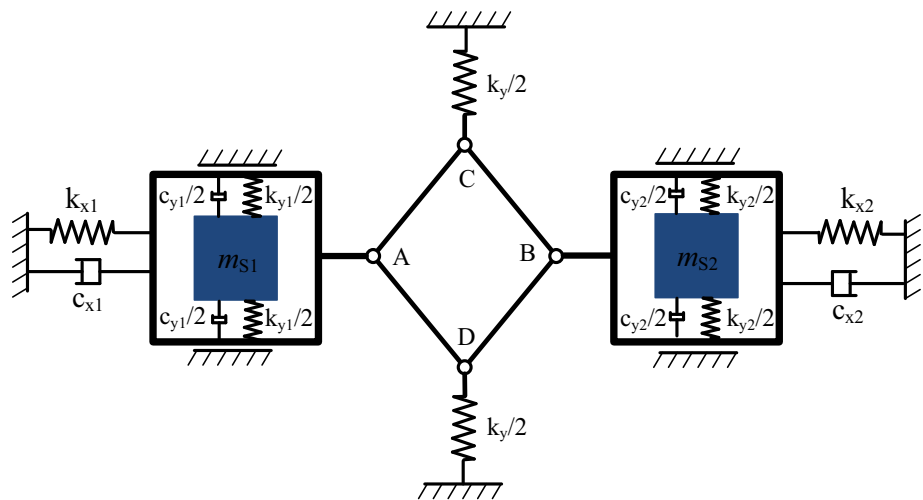
Cross-section of the beams

5 - The anchors
6 - The elastic beams
7 - The rigid beams with the flexible stem
8 - The flexible stem

2D a quarter sketch

Fig. 3 Physical model of the TFG

Table 1 The parameters of the proposed TFG

Design parameters	Value
Dimensions of TFG ($x \times y$)	5500×1930 μm
Thickness of structure	60 μm
Surface area of the proof-mass	$10{,}086 \times 10^2$ μm²
Surface area of the outer frame	9774×10^2 μm²
Length of the drive springs	500 μm
Width of the drive springs	18 μm
Length of the sense springs	510 μm
Width of the sense springs	16 μm
Length of the diamond frame	650 μm
Length of the flexible beam of the connecting frame	300 μm
Mass of the outer frame	1.3664×10^{-7} kg
Sensing mass	1.41×10^{-7} kg
Single gyroscope mass	2.7765×10^{-7} kg
TFG total mass	5.914×10^{-7} kg

Table 2 The properties of Silicon

Property	Value	Unit
Density	2330	kg/m³
Poisson's ratio	0.28	1
Young's modulus	169×10^9	Pa
Bulk modulus	1.2879×10^5	Pa

Table 3 The major modes of the proposed TFG

Vibration modes	Frequency (Hz)
In-phase sensing mode	11,479
Anti-phase sensing mode	11,582
Anti-phase driving mode	11,605

four other elastic beams 4. Each of these beams 4 is linked to the substrate (not be presented in Fig. 1) by an anchor 5 to allow the outer frame and the proof-mass to move freely in two perpendicular directions. Two single gyroscopes are connected through a diamond-shaped frame to create the proposed TFG. This frame has four rigid bars 7 with length L and the rectangular cross-section $b \times h$, where h and b are the thickness and width of each bar, respectively. The bars are connected to the connectors by elastic stems 8 with the width s (where $s < b$). The configuration and dynamics analysis of this frame is shown in Fig. 2.

Figure 3 describes a physical model of this TFG, where k_{x1}, k_{x2}, k_{y1}, and k_{y2} are the equivalent stiffness of the elastic beams; c_{x1}, c_{x2}, and c_{y1}, c_{y2} are damping coefficients in x- and y-direction; m_{S1} and m_{S2} are values of the proof-masses; and m_{f1} and m_{f2} are masses of the outer frames.

The points (e.g. A, B, C, and D) are the nodes of the diamond-shaped frame.

3 FEM analysis

The parameters of this TFG is shown in Table 1, and the specific material parameters of Silicon are shown in Table 2.

The governing equations when carrying out the modal analysis are formed as:

$$[M]\{\ddot{q}\} + [C]\{\dot{q}\} + [K]\{q\} = \{0\} \tag{1}$$

where $[M]$-masses matrix; $[C]$-damping matrix; $[K]$-stiffness matrix; and $\{q\}$-deformation vector.

In this paper, the ANSYS software is used to create, analyze and simulate the presented model in Fig. 1. The mesh model for the beams is controlled by using elements with a size of 25 μm, whereas the rest of this MVG is defined by using maple face meshing with 500 μm of an element size to reduce element quantity. The finite element type in this model is SOLID 187 (element 3D with 10 nudes). The element quantity for MVG is 16,915.

3.1 Modal analysis

Three major frequencies of this TFG are shown in Table 3.

The natural vibratory modes of this TFG are displayed in Fig. 4.

The harmonic response is carried out to re-determine the resonant frequency of the structure when applying the exciting force on it. The unit forces are applied to the two outer frames of the TFG in the driving direction (1 μN). To reduce time of the calculation, the range of exciting frequency is chosen in $11.2 \div 12$ kHz and the step of the

(a) The in-phase sensing mode

(b) The anti-phase sensing mode

(c) The anti-phase driving mode
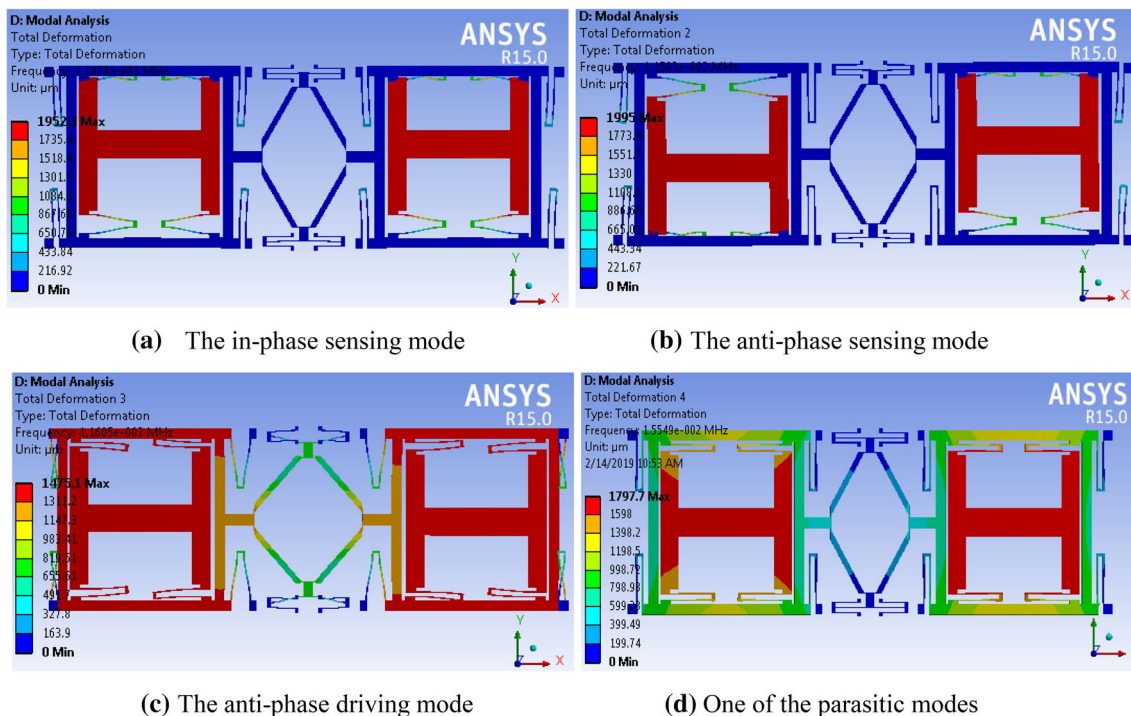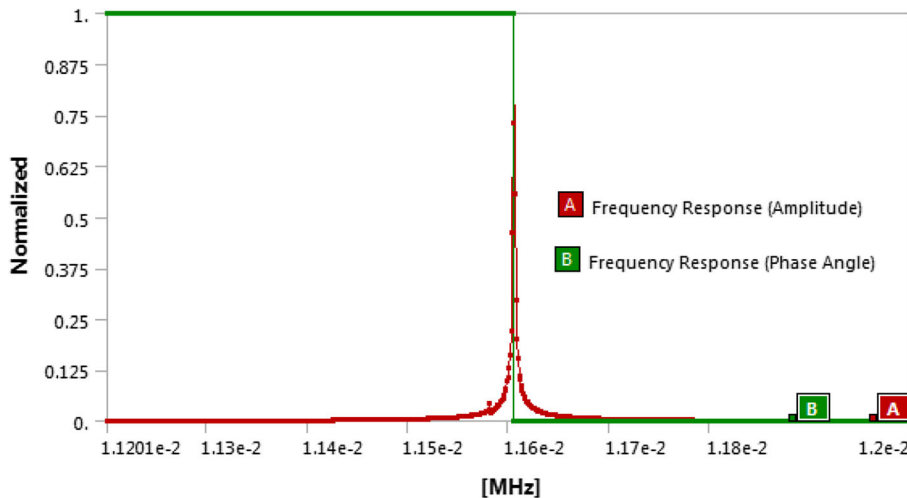
(d) One of the parasitic modes

Fig. 4 Some of the natural vibratory modes of the proposed TFG

Fig. 5 Harmonic response of the proposed TFG

frequency is 10 Hz. The harmonic response of the model is shown in Fig. 4.

The resonant frequency in the driving direction obtained from this analysis is 11,610 Hz (Fig. 5) and match with the result in the modal analysis mentioned above. So, the exciting frequency of the external force applied in this TFG should be chosen following this result.

3.2 Equivalent stiffness

The equivalent stiffness of the flexible beams in driving and sensing direction and the connecting frame is determined using simulation analysis in ANSYS. The unit force (1 μN) is applied on the structure, and the equivalent stiffness is defined from the relation between the deformation and the external force as the formula:

$$k = \frac{F}{\delta} \qquad (2)$$

Fig. 6 Determining the equivalent stiffness of the proposed TFG
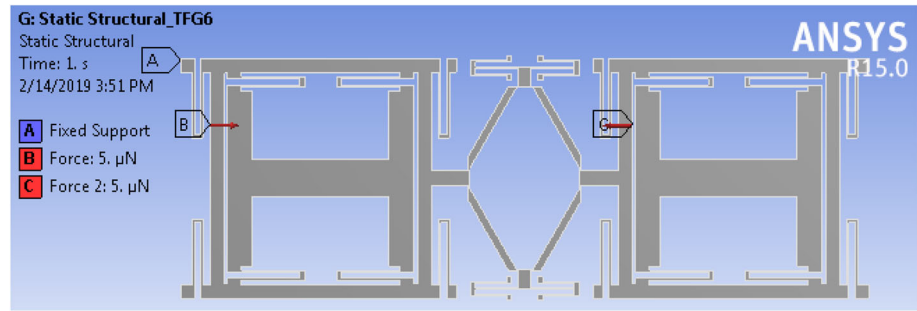
(a) Schemas of applying unit forces on the whole TFG structure
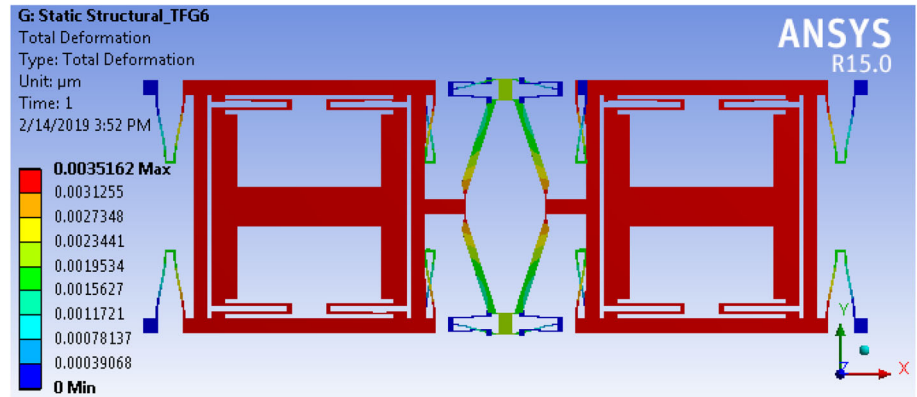
(b) Deformation of the connecting frame with applied unit forces

Table 4 The stiffness of the structures

The structure	Value (N/m)
Stiffness of driving beams	858
Stiffness of sensing beams	725
Stiffness of the connecting diamond-shaped frame	4720
Stiffness of the whole structure in the x-direction	1427

where δ is the deformation of the structure after applying the external force F.

The schemas of applying the external forces on the structures mentioned above are the same and shown in Fig. 6.

As follow the formula (2), the equivalent stiffness of the flexible beams in driving, sensing direction and diamond connecting frame is shown in Table 4.

4 The differential equation of motion

The bars 7 are assumed as a rigid body. The displacement at the end of the beams (A, B, C, and D) is carried out by the elasticity of stems with the smaller section. When the diamond-shaped frame links two single gyroscopes to create the tuning fork structure, points A and B only displace in x-direction and points C and D only do in the y-direction. The displacement of point A is x_1, while point C displaces y_1 from the initial position. Points B and D are the same displacements with A and C point except for the direction of motion (Fig. 3). These displacements depend mutually and are related by the followed formulas:

$$
\begin{cases}
y_1 = \sqrt{L^2 - (L_1 - x_1)^2} - L_2 \\
y_2 = \sqrt{L^2 - (L_1 - x_2)^2} - L_2
\end{cases} \tag{3}
$$

where $L_1 = L\cos\alpha_0$, $L_2 = L\sin\alpha_0$, and α_0 is the angle to define the initial position of rigid bars of the diamond-shaped frame.

Thence the elastic forces are defined by the followed expressions:

$$F_{Dy} = k_y y_D / 2 = k_y y_1 / 2 \tag{4}$$

$$F_{Cy} = k_y y_C / 2 = k_y y_2 / 2 \tag{5}$$

The elastic force applied to the outer frames in the x-direction is determined as the followed expression:

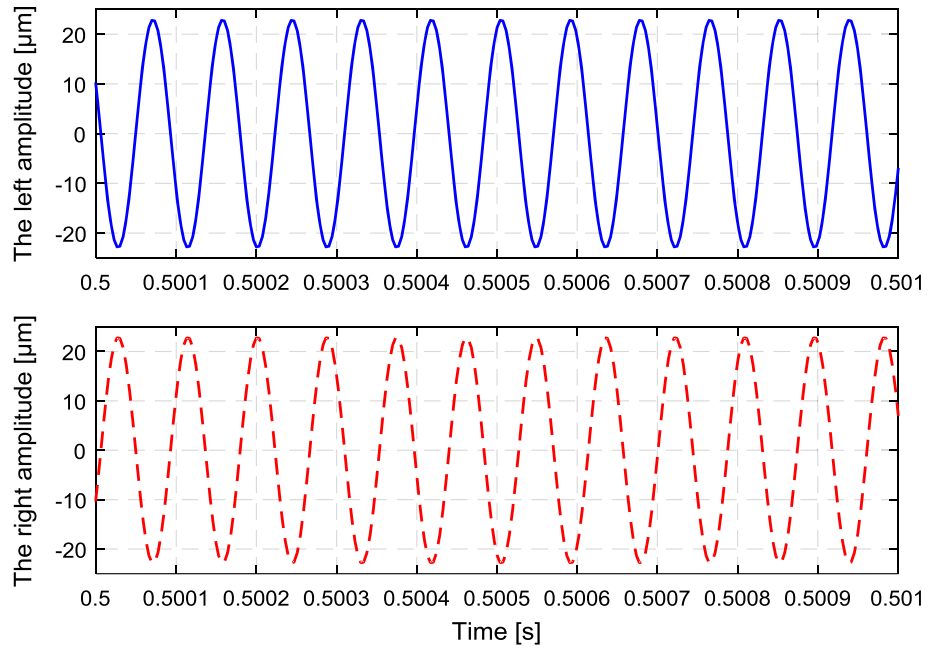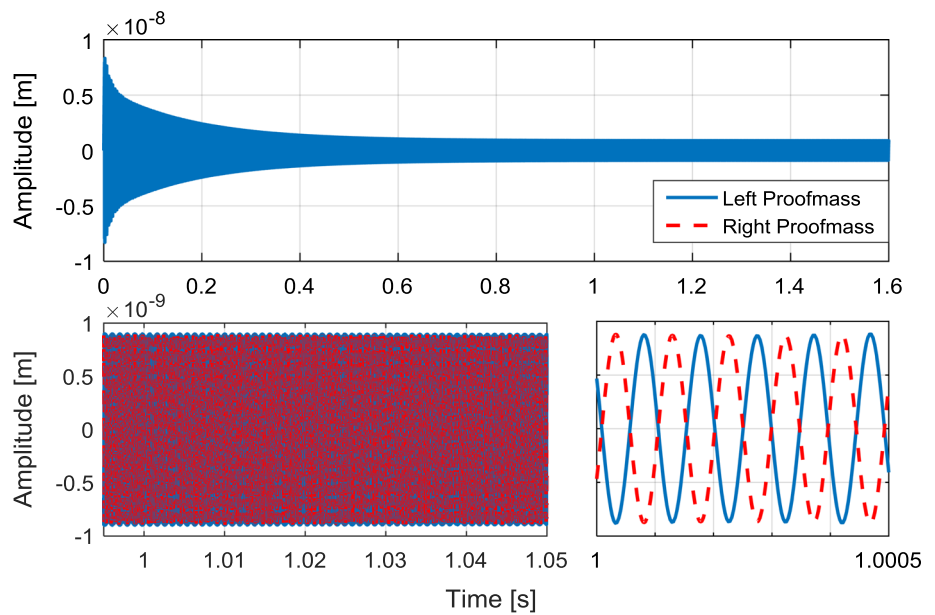**Fig. 7** Mechanical response of two outer frames with deviation phase $\alpha = 0$

Fig. 8 Sensing response with the constant angular velocity

$$F_x = \frac{1}{2}(F_{Cy} + F_{Dy})\cot g\alpha \qquad (6)$$

with α is an angular rotation of a rigid beam when the diamond-shaped frame operating.

By using the second Newton law, the differential equations of motion for the system are obtained as follows:

$$\begin{cases} m_1\ddot{\vec{x}}_1 = \vec{F}_{L1} + \vec{F}_{C1} + \vec{F}_x + \vec{F}_1 \\ m_2\ddot{\vec{x}}_2 = \vec{F}_{L2} + \vec{F}_{C2} + \vec{F}_x + \vec{F}_2 \\ m_{s1}\ddot{\vec{y}}_1 = \vec{F}_{L1} + \vec{F}_{C1} + \vec{F}_1^C \\ m_{s2}\ddot{\vec{y}}_2 = \vec{F}_{L2} + \vec{F}_{C2} + \vec{F}_2^C \end{cases} \qquad (7)$$

Adding some expressions described the relations between the geometrical parameters of the diamond-shaped frame, the differential equations of motion for the whole TFG system becomes as the followed equations:

Fig. 9 The sensing response with the different forms of angular velocity

(a) Trapezoidal angular velocity

(b) Triangular angular velocity
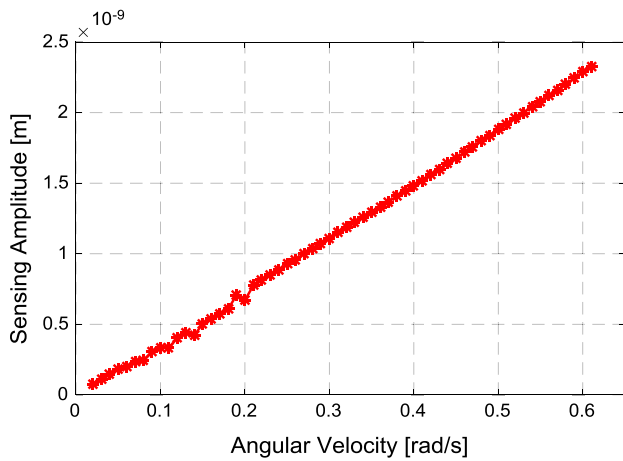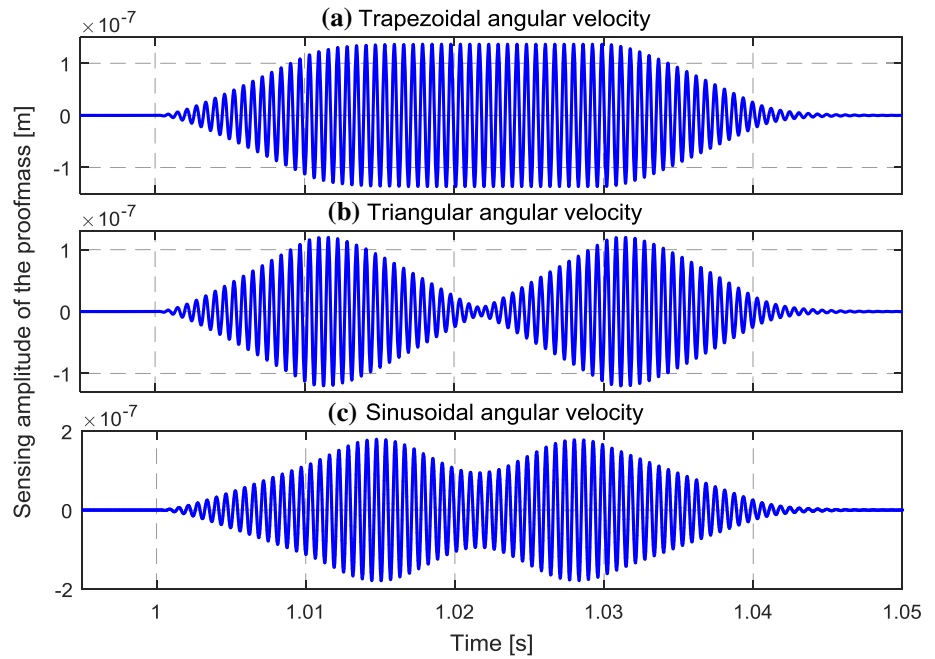
(c) Sinusoidal angular velocity

Fig. 10 The linear dependence of the sensing displacement on the angular velocity

$$\begin{cases} m_1\ddot{x}_1 + c_{x1}\dot{x}_1 + k_{x1}x_1 \\ \quad + \frac{1}{4}k_y\left(\sqrt{L^2 - (L_1 - x_1)^2} + \sqrt{L^2 - (L_1 - x_2)^2} - 2L_2\right) \\ \quad \cot g\alpha = F_1 \\ m_2\ddot{x}_2 + c_{x2}\dot{x}_2 + k_{x2}x_2 \\ \quad + \frac{1}{4}k_y\left(\sqrt{L^2 - (L_1 - x_1)^2} + \sqrt{L^2 - (L_1 - x_2)^2} - 2L_2\right) \\ \quad \cot g\alpha = F_2 \\ m_{s1}\ddot{y}_1 + c_{y1}\dot{y}_1 + k_{y1}y_1 = 2m_{s1}\Omega\dot{x}_1 \\ m_{s2}\ddot{y}_2 + c_{y2}\dot{y}_2 + k_{y2}y_2 = 2m_{s2}\Omega\dot{x}_2 \\ L_1 = L\cos\alpha_0 \\ L_2 = L\sin\alpha_0 \\ \alpha = \text{atan}\left(\frac{\sqrt{L^2 - (L_1 - x_1)^2} - L_2}{x_1}\right) \end{cases} \quad (8)$$

The Eqs. (8) are used to study the response of TFG with every different initial condition.

5 Output mechanical characterization of the TFG

The excited driving forces applied on two outer frames are reversed in the direction (anti-phase) to allow the anti-phase driving mode to appear in this TFG. Two outer frames will oscillate with the same amplitude but reversal phase.

The external forces maybe not completely symmetrical. The phase between them maybe not fully reversal (π radian). Even, there is a difference in the value of the amplitude for them. To express this situation, the deviation phase β is added in the expression of F_l while F_{-r} is kept stably. The deviation phase β describes the non-absolutely opposite level of two exciting forces. Thence, these forces are formed as follow:

$$\begin{aligned} F_l &= F_{0l}\sin(2\pi ft + \beta) \\ F_r &= F_{0r}\sin(2\pi ft + \pi) \end{aligned} \quad (9)$$

where, F_{0l} and F_{0r} are the value of exciting force amplitude applied on the left and right outer frame, f is the resonant frequency in driving direction (defined in harmonic analysis $f = 11{,}600$ Hz). The value of the force is set up to match with the configuration presented in Fig. 1 (i.e. less than 50 μm in this configuration). Thence, the value of the forces, in this case, should be as 60 μN.

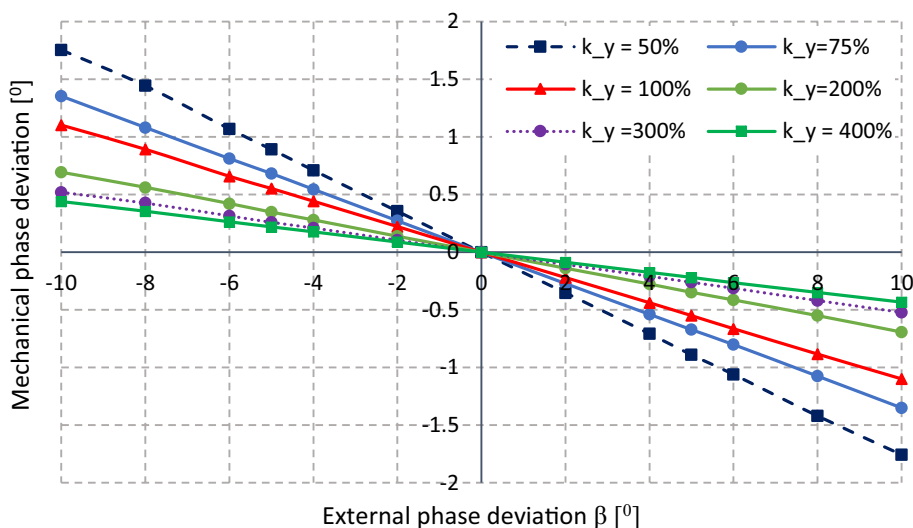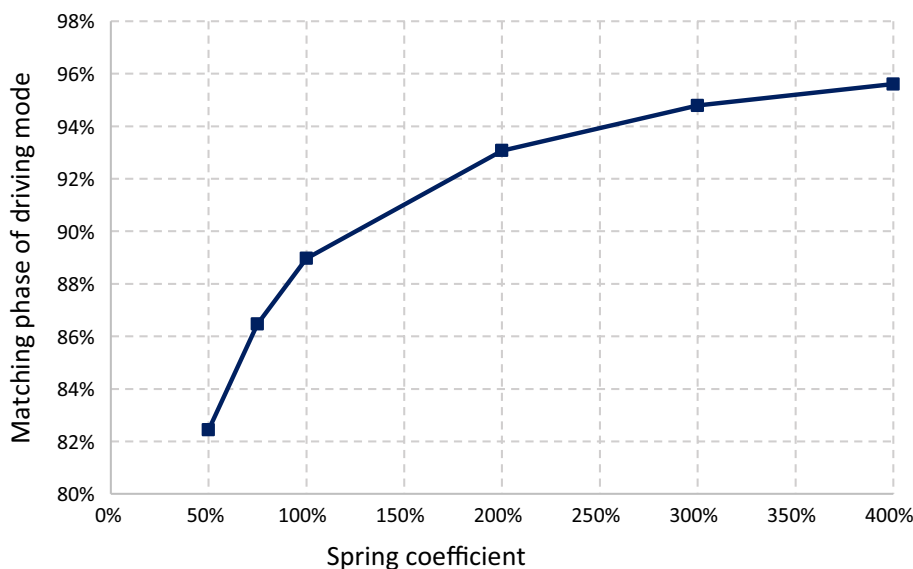**Fig. 11** Mechanical phase deviation of the two outer frame

Table 5 The phase deviation compensation ability in the driving direction

Spring coefficient of the diamond frame	50%	75%	100%	200%	300%	400%
Driving mechanical phase deviation (^{0})	1.76	1.35	1.1	0.69	0.52	0.44
Matching phase in driving mode	82.4%	86.5%	89%	93.1%	94.8%	95.6%

Fig. 12 Matching phase in the driving direction

In the case of $\beta = 0$ and $F_{0r} = F_{0l}$, two exciting forces are absolutely opposite in the anti-phase situation, and the mechanical response of two outer frames are in the anti-phase mode (shown in Fig. 7).

The response of the proof-masses appears in the sensing direction when applying the angular velocity Ω thanks to the Coriolis force with the followed expression:

$$F_C = 2m_s\Omega\dot{x} \tag{10}$$

The function of the angular velocity is formed as the constant, the linearity or the impulse (triangular, trapezoid,

sinusoidal,... mode). The sensing response with the constant Ω form is revealed in Fig. 8. The border of the amplitude of this vibration is straight line after 0.5 s ($0 \div 0.5$ s is a period in which the driving and sensing vibration is unstabilized). The maximal value of the stable amplitude is directly proportional to the applying angular velocity. Besides that, when applying the different forms of the angular velocity on the whole system, the sensing response reflects the form of the applying angular (see Fig. 9). The results show that the TFG model is able to

Fig. 13 Mechanical phase deviation in the sensing direction
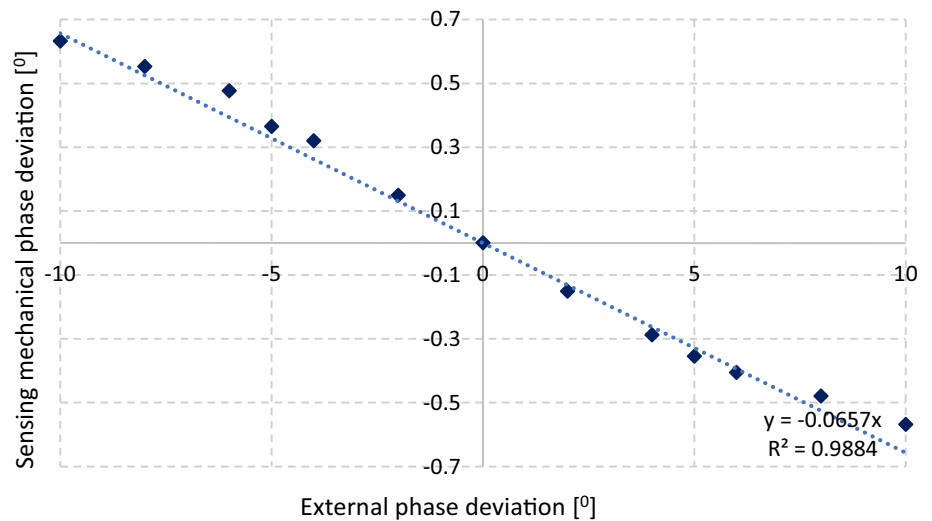
reflect correctly the angular velocity needed to be measured.

The output characterization of this TFG with the constant angular velocity is shown in Fig. 10. The relation between the displacement in the sensing direction and the angular velocity is nearly linear. The variability of the capacity ΔC between the two plates in the TFG depends linearly on the sensing displacement of the proofmass (Acar 2009) as the expression (11). Thence, the variable capacity is directly proportional to the angular velocity.

$$\Delta C = 2N \frac{\varepsilon_0 tL}{d^2} y \tag{11}$$

(N is the number of the moveable combs, ε_0 is the permittivity of the free space, t and L is the structural thickness and overlap length respectively, d is the plate gap and y is sensing displacement of the proofmass). The result in Fig. 10 shows that the sensitivity of the model is defined as to be 3.8 pm/rad/s.

6 Matching phase in the driving and sensing mode

In this study, the deviation β is considered in range $-10^0 \div 10^0$) to observe the mechanical response of two outer frames and two proof-masses. Besides, the value of the forces is different on two sides. In every case with different equivalent stiffness of the connecting diamond-shaped frame, the vibration of the outer frame and proof-mass in each tine of TFG is considered and thence let us evaluate the influence of the stiffness of the connecting frame to the ability creating the matching phase between two outer frames of the proposed TFG.

The results in Fig. 11 show that the equivalent stiffness of the connecting frame strongly affects the ability to

match phase in the driving direction of the connecting diamond-shaped frame. The larger the equivalent stiffness of the connecting frame, the lower the driving phase deviation and the higher the phase deviation compensation ability. In the case of the connecting frame mentioned in this paper, the matching phase between two outer frames is defined to be 89% ($1.1^0/10^0$). Besides that, the ability to compensate for the phase deviation in driving increases up to 95.6% when rising the equivalent stiffness of the connecting frame to 4 times. The influence of the equivalent stiffness of the connecting frame to the matching phase in the driving direction is surveyed and displayed in Table 5 and Fig. 12.

The matching phase between two proof-masses in the two tines of TFG structure depends on some factors such as the driving forces, the deflection in the spring coefficient in sensing direction, the noise in the operating process, etc. In this research, the influence of the deflection of the phase between the two driving forces applied to two tines of the TFG model is considered, whereas the others are ignored. The external phase deviation changes in the range mentioned above. The input angular velocity is defined to obtain the required sensing amplitude (according to the survey, this value needs to be about 10 rad/s). The stiffness coefficient of the connecting diamond-shaped frame is still kept to be 4720 N/m as originally. According to the survey, the matching phase in the sensing direction of two proof-masses is displayed in Fig. 13 with the ability to compensate for the sensing phase deviation of the connecting frame as 93.67% (the compensation $0.633^0/10^0$).

7 Conclusion

This paper presents the model design of a MEMS vibratory gyroscope in tuning fork type with the connecting diamond-shaped frame. The dynamic parameters of this system are determined using the finite element method with ANSYS software. The analysis of the matching phase between two tines of this gyroscope in the driving and sensing direction is carried out to confirm the ability of the connecting frame to compensate for the phase deviation appeared from external forces. The results showed that the equivalent stiffness of the connecting frame considerably affects the matching phase of the system. In this case, the matching phase of the gyroscope is about 89% and 93.67% in the driving and sensing mode, respectively. The ability to compensate for the phase deviation in driving mode increases up to 95.6% when the equivalent stiffness of the connecting diamond-shaped frame rises 4 times. This result is an important basis for further researches to improve the configuration of the TFG model and increase the performance of the sensor with this type.

References

Acar C, Shkel AM (2009) Vibratory gyroscopes—structural approaches to improve robustness. Springer, Berlin

Andrei SM (1999) Dynamics and control of micromachined gyroscopes. In: The American control conference, San Diego, California, pp 2119–2124

Apostolyuk V, Tay FEH (2005) Dynamics of micromechanical coriolis vibratory gyroscopes. Sens Lett 2:1–8

Bumkyoo C, Lee SY, Kim T, Baek SS (2008) Dynamic characteristics of vertically coupled structures and the design of a decoupled micro-gyroscope. Sensors 8:3706–3718

Dunzhu X, Cheng Y, Lun K (2014) The development of micromachined gyroscope structure and circuitry technology. Sensors 14:1394–1473

Guan Y, Gao S, Liu H, Niu S (2014) Acceleration sensitivity of tuning fork gyroscopes: theoretical model, simulation and experimental verification. Microsyst Technol 21:1313–1323

Guan Y, Gao S, Haipeng L, Lei J, Shaohua N (2016a) Design and vibration sensitivity analysis of a MEMS tuning fork gyroscope with an anchored diamond coupling mechanism. Sensors 16:468–483

Guan Y, Gao S, Jin L, Cao L (2016b) Design and vibration sensitivity of a MEMS tuning fork gyroscope with anchored coupling mechanism. Microsyst Technol 22:247–254

Huilin S, Yongpeng W (2011) Modeling and simulation for a vibratory tuning-fork MEMS gyroscope. In: Third international conference on measuring technology and mechatronics automation, June 2011, pp 605–608

Sharma A, Zaman FM, Amini BV, Ayazi F (2004) A high-Q in-plane SOI tuning fork gyroscope. Proc IEEE 1:467–470

Shkel AM (2006) Type I and type II micromachined vibratory gyroscopes. In: Proceedings of the IEEE/ION PLANS, San-Diego, USA, pp 586–592

Trinh TQ, Nguyen LQ, Dao DV, Chu HM, Vu HN (2014) Design and analysis of a z-axis tuning fork gyroscope with guided-mechanical coupling. Microsyst Technol 20(2):281–289

Trusov AA, Schofield AR, Shkel AM (2013) Micromachined rate gyroscope architecture with ultra-high quality factor and improved mode ordering. Sens Actuators, A 165(1):26–34

Van The V, Dung TQ, Trinh CD (2018) Dynamic analysis of a single MEMS vibratory gyroscope with decoupling connection between driving frame and sensing proofmass. Int J Appl Eng Res 13(7):5554–5561

Weinberg M, Kourepenis A (2006) Error sources in in-plane silicon tuning-fork MEMS gyroscopes. IEEE/ASME J Microelectromech Syst 15(3):479–491

Yazdi N, Ayazi F, Najafi K (1998) Micromachined inertial sensors. Proc IEEE 86:1640–1659

Yoon SW, Lee S, Khalil K (2012) Vibration-induced errors in MEMS tuning fork gyroscopes. Sens Actuators, A 180:32–44

Zaman M, Sharma A, Hao Z, Ayazi F (2008) A mode-matched silicon-yaw tuning-fork gyroscope with sub-degree-per-hour allan deviation bias instability. J Microelectromech Syst 17(6):1526–1536